Nanoscale Horizons

ROYAL SOCIETY OF CHEMISTRY

COMMUNICATION

View Article Online
View Journal

Cite this: DOI: 10.1039/d6nh00035e

Received 24th January 2026,
Accepted 16th April 2026

DOI: 10.1039/d6nh00035e

rsc.li/nanoscale-horizons

Open Access Article. Published on 25 Abrëll 2026. Downloaded on 29.05.26 17:53:24.
This article is licensed under a Creative Commons Attribution-NonCommercial 3.0 Unported Licence.

Ferroelectricity in wurtzite atomic layer annealed aluminum nitride thin films

Dominic A. Dalba,[a] Dilan M. Gamachchi,[a] Indeewari M. Karunarathne,[a] Bipin Bhattarai,[a] Xiaoman Zhang,[b] Wangwang Xu,[c] Somayeh Saadat Niavol,[a] Dongmei Cao,[c] W. J. Meng[c] and Andrew C. Meng*[a]

Investigation of aluminum nitride-based ferroelectric thin films for non-volatile memory applications has largely focused on various thin film solid solutions grown by reactive sputtering. The growth process leads to significant DC electrical leakage related to mosaic disorder and point defects in this class of materials; extrinsic alloying elements such as scandium or boron are used to facilitate ferroelectric switching at lower electric fields to limit these deleterious effects. We take a different approach focusing on growth *via* atomic layer annealing using a nitrogen remote inductively coupled plasma (ICP). We demonstrate ferroelectric behavior in nanocrystalline wurtzite aluminum nitride (AlN) films with neither additional alloying components nor post-process annealing grown using a 350 °C CMOS-compatible growth process. The films do not exhibit hard dielectric breakdown even under electric fields in excess of 10 MV cm^{-1}. Electrical property characterization using positive-up-negative-down (PUND) measurements shows remanent polarization (P_r) in excess of 30 μC cm^{-2}. Piezoresponse force microscopy (PFM) DC bias poling experiments yield behavior consistent with ferroelectricity. Structural characterization was performed using scanning/transmission electron microscopy, X-ray photoelectron spectroscopy depth profiling, and spectroscopic ellipsometry. An ALD-based growth approach to ferroelectric aluminum nitride-based films holds significant advantage from a device scaling standpoint and provides an alternative route towards aluminum nitride-based thin films.

New concepts

Strong ferroelectric response in wurtzite AlN-based materials is highly promising for non-volatile memory applications. However, very high coercive field nearing the breakdown potential leads to DC electrical leakage related challenges hypothesized to arise from point defects (*e.g.* vacancies). Despite this, most reports focus on reactive sputtered films, in which ion bombardment induced point defects can be difficult to control. We focus on wurtzite AlN growth using atomic layer annealing, a remote plasma assisted atomic layer deposition process, with the goal of lower density of electronic defects. We report an improved breakdown field in excess of 10 MV cm^{-1}. As a result of being able to apply significantly higher electric fields, we observe ferroelectric response in pure wurtzite AlN with no intentional extrinsic alloying. Atomic layer annealed wurtzite AlN-based films also hold significant advantages for integration with silicon-based electronic devices.

Wurtzite aluminum nitride (AlN)-based ferroelectric materials show significant promise for applications in non-volatile memory (NVM) devices.[1–10] These materials are potentially compatible with complementary metal-oxide-silicon (CMOS) processing and have extremely high remanent polarization (P_r) and coercive fields with potential for wide memory window and high memory density devices. Compared to existing high-performance hafnium oxide (HfO_2)-based ferroelectric materials in this application space, wurtzite AlN-based materials hold a fundamental advantage: the ferroelectric wurtzite phase is thermodynamically stable.[11] In HfO_2-based materials, structural transformation between the ferroelectric orthorhombic phase and non-ferroelectric tetragonal and monoclinic phases during processing[12,13] and under applied external electric fields[14–16] is hypothesized to relate to changing ferroelectric response under electrical cycling. These phenomena, termed wake-up[12,16] and fatigue,[17,18] at the respective beginning and end of the device cycle lifetime, are a critical bottleneck to achieving high reliability ferroelectric NVM. The potential to avoid these problems is perhaps the most compelling argument for use of wurtzite AlN-based ferroelectric materials. Wurtzite AlN-based ferroelectric materials have their own unique challenges related to device reliability. For example, AlScN is among the most promising and widely studied of this class of materials;[3,7,9,10] despite ostensibly being a wide-bandgap insulator, it is notorious for DC electrical leakage.[19–21]

To clarify this apparent paradox, we note that wurtzite AlN-based ferroelectrics, such as AlScN, are not electrical conductors in the traditional sense of the term. At electric fields

[a] *Department of Physics and Astronomy, University of Missouri, Columbia, USA. E-mail: acmeng@missouri.edu*

[b] *Department of Engineering and Industrial Professions, University of North Alabama, Alabama, USA*

[c] *Department of Mechanical and Industrial Engineering, Louisiana State University, USA*

Open Access Article. Published on 25 Abrëll 2026. Downloaded on 29.05.26 17:53:24.
This article is licensed under a Creative Commons Attribution-NonCommercial 3.0 Unported Licence.

$\sim$ 1 MV cm^{-1}, these materials are effectively insulators. However, ferroelectric switching requires application of external electric fields that exceed the coercive field, which for wurtzite AlN-based ferroelectrics is very high and typically greater than 3 MV cm^{-1}.[3,22] Thus, the challenge in these materials, more precisely, is that DC electrical leakage is high under high electric fields.[21] The problem is also convoluted by wide-ranging reports of differing DC electrical leakage.

We note most reports of wurtzite AlN-based ferroelectric thin films are grown by reactive sputtering.[1,3,4,9,18,19] For NVM applications, CMOS process compatibility is of paramount importance for integration with Si-based electronic devices. While some reactive sputtering processes technically satisfy the thermal budget requirements,[23] we argue that sputtered films cannot realistically be used for growth of an active layer of an NVM device. From structural considerations, device scaling requirements dictate that the growth process be capable of reproducibly synthesizing films with thicknesses below 10 nm. Sputtering technically satisfies this requirement, but typically proceeds *via* either the Volmer–Weber or Stranski–Krastanov growth mode.[24] Such growths involve island nucleation that leads to structural defects related to high mosaic spread[8,9] (*e.g.*, anomalously oriented grains[25,26]) whose formation is largely stochastic. From electronic property considerations, which are arguably more important, ion bombardment induced point defects in sputtered wurtzite AlN-based thin films[21] are a huge concern. Deleterious effects of point defects on electronic properties remain an open question. System-to-system variation in ion bombardment induced point defect concentrations and spatial distributions provides one possible explanation for wide variations in reported electrical leakage in the literature. Atomic layer deposition (ALD) is a preferred growth process for optoelectronic materials in the semiconductor industry due to precise control over thickness and chemistry and a tendency for lower density of electronic defects at interfaces.[27] There are a few reports of ALD growth of AlN-based ferroelectric materials.[28,29] However, ALD-deposited AlN is typically either amorphous or very weakly crystalline.[30,31] The current work focuses on atomic layer annealing (ALA).[32] ALA is similar to ALD: sequential precursor pulses are separated by purge pulses; however, an additional plasma pulse is used to facilitate densification and crystallization of the film being grown. ALA with Ar plasma has been previously used to successfully grow crystalline wurtzite AlN.[33,34,35]

There is recent controversy over whether pure wurtzite AlN is a ferroelectric material.[36,37] Several recent reports show ferroelectricity in pure wurtzite AlN, while for decades, it was thought that the material was a piezoelectric material that is non-ferroelectric.[36,38–40] Careful examination of this claim shows that it makes no sense: if ferroelectricity in AlScN arises from reversible switching between N- and metal-polar states in the wurtzite nitride crystal structure, then AlN should exhibit the same behavior. The reason for this apparent paradox is related to the key challenge of DC electrical leakage in wurtzite AlN-based ferroelectrics. Because the coercive field is so high, whether or not ferroelectricity is observed depends on whether the coercive field can be reached before DC electrical leakage dominates when the electric field approaches the breakdown field. If there is sufficient separation between the coercive field and the breakdown field, ferroelectricity can be observed in pure wurtzite AlN.

Here, we report ferroelectricity in nanocrystalline wurtzite AlN grown using a 350 °C ALA process. The growth satisfies the thermal budget requirements for back end of line (BEOL) CMOS process compatibility[23] and uses N_2 plasma instead of Ar plasma, which is typically used in ALA processes. We perform comprehensive structural characterization of the AlN thin films using Scanning/Transmission Electron Microscopy (S/TEM), X-ray Photoelectron Spectroscopy (XPS) depth profiling, and spectroscopic ellipsometry. We probe ferroelectric behavior of the AlN thin films using electrical property measurements and piezoresponse force microscopy (PFM).

The growth process of AlN was designed to conform to BEOL CMOS process requirements.[23] Trimethylaluminum (TMA) and hydrazine (N_2H_4) precursors were chosen based on their compatibility with an ALD temperature window below 350 °C.[31] We chose N_2H_4 over more conventional nitrogen precursors (*e.g.* NH_3) due to its high reactivity at low temperatures and tendency for increased nitrogen incorporation.[34] Growth was performed on Si(111) substrates without removing the native oxide. Si(111) substrates with native oxide were initially cleaved and cleaned sequentially using nitric acid (15.8 M), isopropanol, and ethanol, followed by a DI water rinse and dried with compressed air. Growth was also performed on 30 nm thick electron transparent SiN_x window plan-view TEM grid samples (Electron Microscopy Sciences). Thin film growth using ALA was performed using an Anric Technologies AT650P plasma ALD system equipped with a remote inductively coupled plasma (ICP). The system is pumped using a rotary vane pump (Welch, Fomblin CRVpro 16) and has an ultimate base pressure in the few mTorr range. ICP is chosen for control over plasma

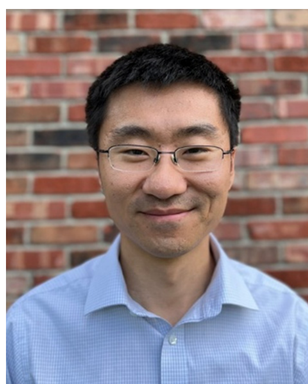

Andrew C. Meng

Andrew Meng is an Assistant Professor in the Department of Physics and Astronomy at the University of Missouri, Columbia. He graduated with a BS in Physics and Chemistry from Caltech in 2013. In 2014, Andrew earned an M.Phil. in Chemistry from the University of Cambridge as a Churchill Scholar. Andrew received his PhD and MS in Materials Science and Engineering in 2019 from Stanford University working on CVD growth of germanium-tin nanowires. Andrew's research interests include semiconductor crystal growth for functional device applications and structural characterization using electron microscopy. Andrew's first paper as an independent investigator was published in Nanoscale Horizons in 2023. Congratulations to Nanoscale Horizons on its 10th anniversary.

Open Access Article. Published on 25 Abrëll 2026. Downloaded on 29.05.26 17:53:24.
This article is licensed under a Creative Commons Attribution-NonCommercial 3.0 Unported Licence.

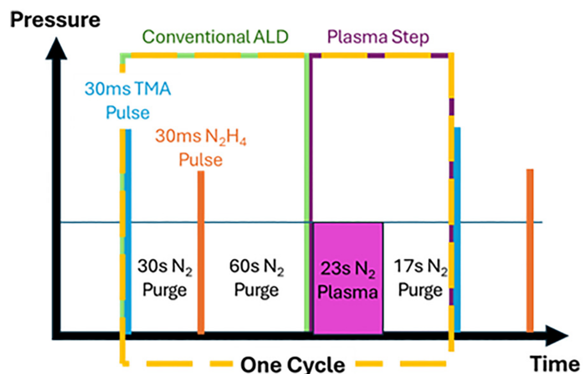

Fig. 1 Cycle sequence of AlN deposited using N_2 plasma process.

density through plasma power without significant changes to plasma potential and ion flux, which can lead to ion-bombardment induced electronic defects.[41] The substrate temperature was set to 350 °C and allowed to stabilize prior to the growth. The ALA process consists of a supercycle of 3 pulses separated by N_2 carrier gas purge pulses: TMA, N_2H_4, and N_2 plasma (Fig. 1). The TMA and N_2H_4 precursor pulse times were set to 30 ms, followed by purge times of 30 s and 60 s, respectively. The N_2 plasma (100 W rf input power) pulse time was set to 23 s, followed by a purge time of 17 s. N_2 carrier gas flow was set to 15 sccm. To probe electrical behavior of the AlN films, we fabricated capacitor test structures. The degenerately doped Si substrate was used as the bottom electrode, and circular Pt top electrodes (120 nm thick) were then deposited through a shadow mask with 500 μm diameter holes on a square pitch in a sputter coating system (Quorum, 150TES).

Plan-view TEM samples were characterized as-grown. Cross-section TEM samples were fabricated using a ThermoFisher Helios Hydra plasma focused ion beam (PFIB)/scanning electron microscope (SEM). A regular cross section was cut using Xe^+ ion source at 30 kV accelerating voltage. The ion source was switched to Ar^+ after the sample was lifted out and attached to a Cu TEM lift-out grid (Ted Pella). The sample was thinned at successively lower beam currents and accelerating voltages, with final thinning performed at 5 kV.

Film thicknesses of samples grown on native oxide on Si(111) substrates were determined as a function of incident wavelength using a variable angle spectroscopic ellipsometer (J.A. Woolam, VB-400 with 75 W convection cooled Xe light source and HS-190 high speed monochromator system). Surface and bulk film composition was measured using XPS depth profiling using a Scienta Omicron ESCA 2SR X-ray Photoelectron Spectroscope with a monochromatic Al Kα excitation source. XPS spectra were acquired from AlN films as-grown and after sputter etching with a 4.5 kV 2 μA Ar^+ ion beam for 0–60 min. Raw XPS data were processed using CasaXPS. S/TEM characterization was performed using a probe aberration corrected ThermoFisher Spectra 300. High resolution TEM (HRTEM) imaging and STEM imaging were performed at 300 kV accelerating voltage. Differential phase contrast (DPC) imaging in STEM was performed at 145 mm camera length using a segmented detector (ThermoFisher, Panther). The microscope is equipped with a Super-X X-ray Energy Dispersive Spectroscopy (EDS) silicon drift detector system with a 0.7 sr solid angle. STEM-EDS mapping was performed at spot size 7 (∼150 pA beam current).

The electrical behavior of 500 μm diameter capacitors were measured using a Keithley 4200-SCS semiconductor parameter analyzer. Positive-up negative-down (PUND) measurements, in which a negative polarity voltage reset pulse preceded two positive voltage pulses followed by two negative voltage pulses to probe the forward and reverse polarization and leakage currents, respectively, were performed with triangle pulses (rise/fall time = 100 μs, delay = 100 μs). The polarization-voltage response was obtained from the PUND data by subtracting the leakage/parasitic current pulses (U, D) from the polarization switching current pulses (P, N) and then integrating current with respect to time and dividing by device area to yield polarization.

PFM DC poling experiments were performed using a Bruker Dimension Icon atomic force microscope (AFM) equipped with the PFM module. A 10 V drive amplitude with a 7 kHz AC bias wave was used to probe piezoresponse amplitude and phase. Poling was performed by applying a DC bias of +35 V and −35 V in a square-in-square geometry to the AFM tip with respect to the grounded sample chuck during a PFM scan with a 100 mV AC bias. PFM measurements of a larger area containing the poled regions were performed after applying DC bias to show residual changes to piezoresponse.

Spectroscopic ellipsometry was used to determine the thickness of ALA AlN films (Fig. 2). The growth rate was determined to be approximately 0.9 Å $cycle^{-1}$. XPS depth profiling was used to characterize the elemental composition of the AlN films. Fig. 3 shows that the ALA AlN films are composed mainly of Al and N. Trace amounts of C and O are found uniformly throughout the film at ∼4 at%. The measured Al to N ratio is significantly less than stoichiometric at approximately 1 : 0.64, indicating that the films are nitrogen-poor. Even accounting for oxygen as a potential counterion, the Al to N to O ratio is 1 : 0.64 : 0.08. This value is likely being affected by changes in sputter yield due to sample geometry and matrix effects.[42]

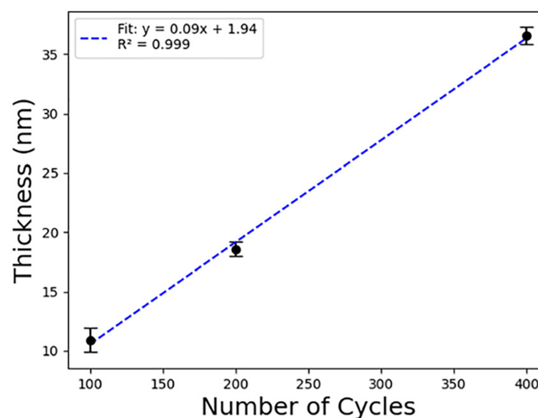

Fig. 2 Thickness dependence on growth cycles as measured by spectroscopic ellipsometry.

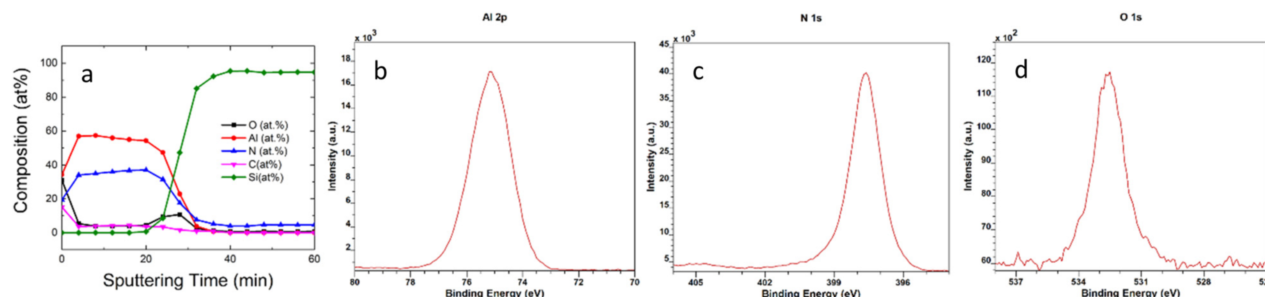

Fig. 3 Atomic layer annealed AlN (a) XPS depth profile, and detailed XPS core level scans (b) Al 2p, (c) N 1s and (d) O 1s signals.

Open Access Article. Published on 25 Abrëll 2026. Downloaded on 29.05.26 17:53:24.
This article is licensed under a Creative Commons Attribution-NonCommercial 3.0 Unported Licence.

Thus, we perform additional compositional analysis in S/TEM for a more complete picture. Despite the sub-stoichiometric Al to N ratio measured using XPS depth profiling, we note that the N : O ratio measured using this method is 16× higher in ALA AlN films (8 : 1) as compared to aluminum oxynitride (AlON) films grown using plasma enhanced ALD (1 : 2),[43] indicating a high degree of nitrogen incorporation of the ALA process. High resolution XPS core level scans after 12 min of Ar^+ sputtering are shown in Fig. 3b–d. The main features are a single Al 2p peak at ∼75 eV, an N 1s peak at 397.5 eV, and O 1s peak at 532.5 eV.

Structural characterization was performed using S/TEM. We first characterized ALA thin films grown directly on electron-transparent SiN_x window plan-view TEM grids. HRTEM imaging (Fig. 4a and b) shows randomly oriented wurtzite nanocrystals. The lateral grain size is on the order of a few nm to ∼10 nm. The Fast Fourier Transform (FFT) shows, in addition to the [100] zone axis pattern of the unetched part of the Si(100) substrate below the SiN_x, the polycrystalline diffraction rings from the (100), (002), (101), (102), (110), (103), and (200) reflections of wurtzite AlN (Fig. 4c). The additional satellite polycrystalline diffraction rings arise from dynamical diffraction. Because the ALA AlN thin film is deposited directly onto the electron transparent SiN_x window, no additional sample preparation is required as long as the total thickness is less than ∼100 nm. Thus, the HRTEM data from the plan-view ALA AlN sample verifies that the sample is crystalline as-grown without artifacts introduced by cross-section sample fabrication using FIB. Furthermore, the plan-view geometry provides a view of lateral grain/domain size that is not influenced by FIB sample thinning.

The cross-section HRTEM image (Fig. 5a) shows the single crystal Si(111) substrate along a [110] zone axis orientation, the ALA polycrystalline wurtzite AlN thin film, and the protective W cap deposited by electron- and ion-beam induced deposition in the FIB during sample fabrication. The inset shows lattice fringes in a wurtzite AlN nanocrystal (Fig. 5a). The FFT shows polycrystalline diffraction rings from the (100), (002), (101), (102), (110), (103), and (200) reflections of wurtzite AlN in addition to the [110] zone axis diffraction pattern from the Si(111) substrate (Fig. 5b). A high angle annular dark field (HAADF) STEM image and STEM-EDS maps are shown in Fig. 5c–f. The Al and N signals from the ALA AlN film are approximately uniform (Fig. 5d and e). We observe that most of the O signal is observed in the Si(111) substrate native oxide and in the W cap; there is very little O signal from the AlN film (Fig. 5f), consistent with XPS depth profile data.

Differential phase contrast (DPC) imaging in STEM[9,44,45] is used to characterize ferroelectric domains (Fig. 6c and d). In this imaging mode, deflection of the electron beam (due to local electromagnetic fields from polarizations, or changes in crystallographic orientation) is measured by a segmented STEM detector, which captures differences in scattered electron

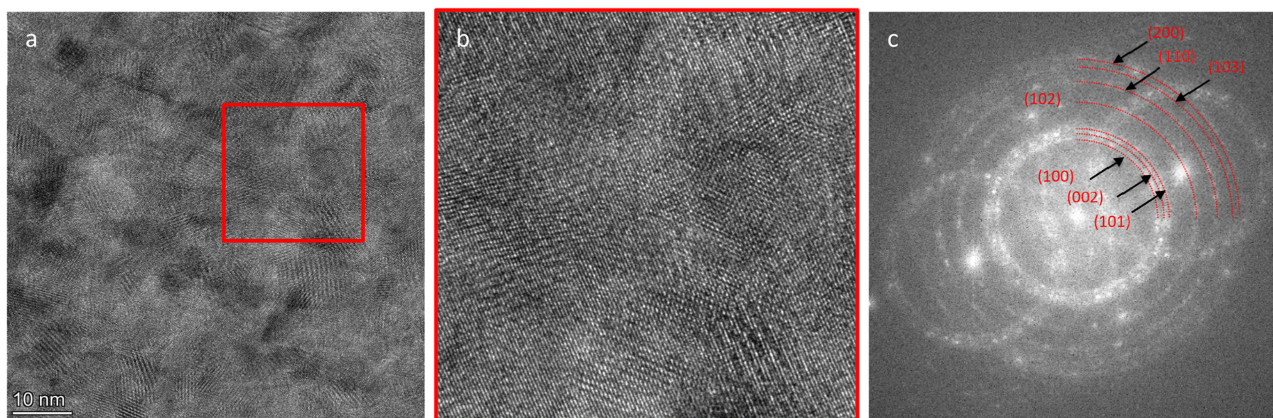

Fig. 4 Plan-view ALA wurtzite AlN thin film deposited on electron transparent SiN_x TEM grid (a) HRTEM, (b) inset, (c) FFT. The Si(100) zone axis diffraction pattern arises from unetched part of the Si(100) substrate used to fabricate the electron transparent SiN_x membrane samples.

 This journal is © The Royal Society of Chemistry 2026

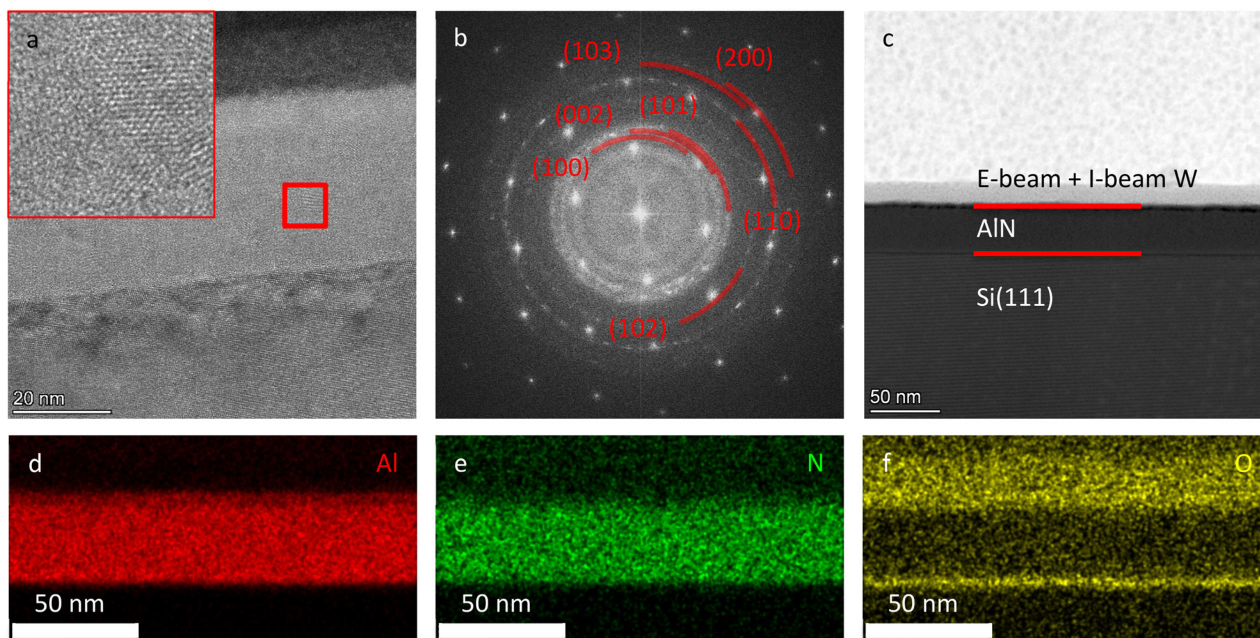

Fig. 5 Cross-section ALA wurtzite AlN thin film deposited on Si(111) (a) HRTEM, (b) FFT, (c) HAADF-STEM image, and STEM-EDS maps showing (d) Al, (e) N, and (f) O signal intensities.

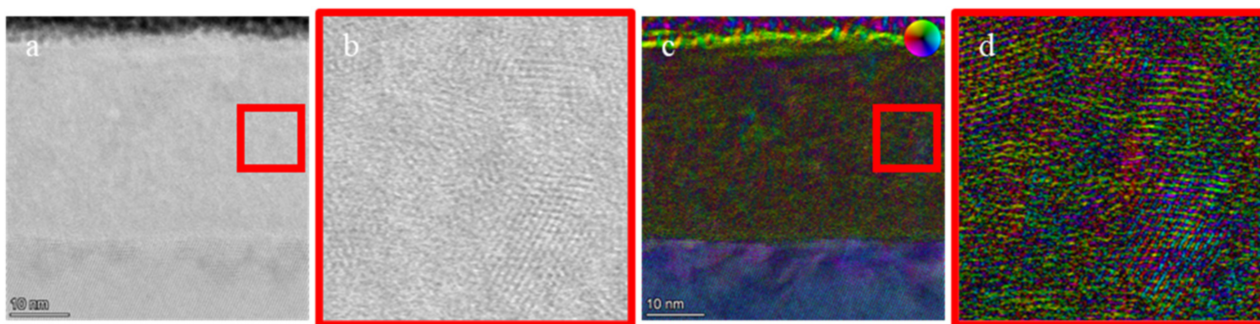

Fig. 6 Atomic layer annealed wurtzite AlN thin film (a) BF STEM image and (b) inset, (c) STEM-DPC image and (d) inset.

Open Access Article. Published on 25 Abrëll 2026. Downloaded on 29.05.26 17:53:24.
This article is licensed under a Creative Commons Attribution-NonCommercial 3.0 Unported Licence.

intensity in two perpendicular component directions. The magnitude and orientation of the deflection yields a vector, which is represented by intensity and color, respectively. Furthermore, while crystallographic orientation changes can induce DPC, we emphasize that for wurtzite AlN, ferroelectric polarization changes are fixed with respect to crystallographic orientation changes and *vice versa*. For example, rotating a N-polar wurtzite AlN nanocrystal by 180° not only changes crystallographic orientation, but also changes the polarization to Al-polar. Because atomic resolution is attained in the bright field (BF) STEM image (Fig. 6a and b), atomic columns are also visible in the STEM DPC image (Fig. 6c and d) from the same region. In addition to contrast from the atomic columns, we observe variation in the polarization over a longer length-scale ~ few nm. Comparing the inset of the BF STEM image (Fig. 6b) with that of the STEM DPC image (Fig. 6d), this longer length-scale variation of polarization is consistent with domain contrast coinciding with grain boundaries.

Ferroelectric properties of AlN thin films were characterized using PUND measurements at room temperature. Fig. 7a shows leakage current-corrected polarization-electric field (P–E) characteristics of a high polarization, 35 nm thick, ALA wurtzite AlN capacitor device with $2P_r \sim 70\ \mu C\ cm^{-2}$. Raw P, U, N, and D current transients with identical axes are shown for two high polarization devices (Fig. S1 and S2) and an average polarization device (Fig. S3) in the Supporting Information. For different PUND waveforms, we do not observe a significant delay time dependence (Table S1). There is a significant increase in polarization current as a function of increased pulse time (Table S2a). This effect is avoided by using the shortest possible pulse time allowed by the data sampling rate (triangle wave). We attribute the increase in polarization current as a function of pulse time to polarization-dependent leakage. If we exclude the increase in polarization current during the constant voltage part of a trapezoidal pulse, no significant change in polarization is observed (Table S2b). The primary source of uncertainty

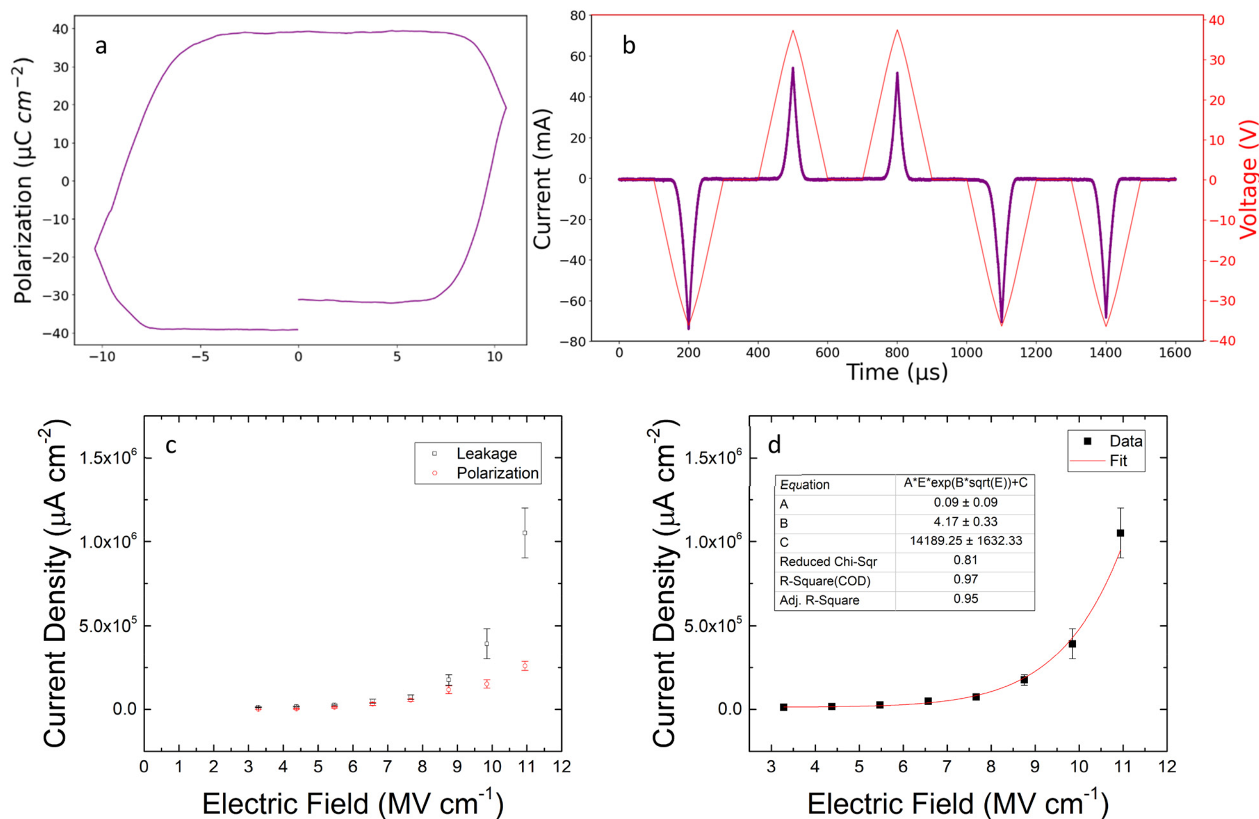

Fig. 7 High remanent polarization ferroelectric capacitor (a) leakage-corrected polarization-electric field characteristics, (b) PUND measurement, (c) comparison of polarization (red circles) and leakage currents (black squares), and (d) fit of leakage current to Poole–Frenkel equation (red trace) to experimental data (black squares).

Open Access Article. Published on 25 Abrëll 2026. Downloaded on 29.05.26 17:53:24.
This article is licensed under a Creative Commons Attribution-NonCommercial 3.0 Unported Licence.

in P_r is device-to-device variation; subtraction error (Fig. S1–S3) is comparably small. Fig. 7b shows the PUND measurements from which the P–E characteristics were constructed. AlN exhibits an average $2P_r$ of 52 ± 11 μC cm^{-2} (sample size, 20 devices) when an electric field of approximately 10 MV cm^{-1} is applied. Here the high polarization device has a P_r that is approximately 70% of the theoretical remanent polarization;[8] on the other hand we report extremely high applied electric fields of 10 MV cm^{-1} without hard dielectric breakdown. The retention data is shown in the SI (Fig. S4). We note that asymmetry in P–E characteristics has been previously observed in wurtzite nitride-based ferroelectric materials;[46] we hypothesize that this imprint effect may also be attributed to the bottom electrode. However, ALA growth on other bottom electrode substrates is beyond the scope of the current work.

Despite the high P_r we observe that the PUND data shows significant DC electrical leakage. Fig. 7c shows a plot comparing leakage current and polarization current. We observe that the leakage current increases significantly as a function of the external applied electric field, especially above 8 MV cm^{-1}, and that a majority of the total current is comprised of leakage contributions. Fitting the functional form of the leakage current to that of Poole–Frenkel emission, or electrical conduction mediated by trap-assisted charge carrier hopping, yields a coefficient of determination $R^2 = 0.97$. This result is consistent with our assertion that the DC electrical leakage problem in wurtzite AlN ferroelectric is not related to conventional charge carrier transport but rather to the uniquely high electric fields required for ferroelectric switching in these materials. In our ALA growth process for wurtzite AlN, we have increased the dielectric breakdown field to above 10 MV cm^{-1}, enabling observation of ferroelectricity in pure wurtzite AlN without intentional extrinsic alloying components.

While there is likely contribution to electrical conduction from multiple mechanisms, including Schottky emission and space-charge limited conduction, the role of high switching fields and non-stoichiometry of the films are consistent with Poole–Frenkel emission as the primary driving force for the high observed leakage. Additional TEM data consistent with the presence of point defects in ALA wurtzite AlN is provided in the Supporting Information (Fig. S5 and S6). We hypothesize that nitrogen vacancies act as positively charged donor-like traps that create deep Coulombic potential wells. Rapid polarity reversal and large transient currents of high electric field ferroelectric switching cause electrons to continually be captured and emitted from these trap states leading to defect driven endurance failure due to domain wall pinning and internal field formation. This leakage current would be directly related to both the applied electric field amplitude and concentration of vacancies.

This journal is © The Royal Society of Chemistry 2026

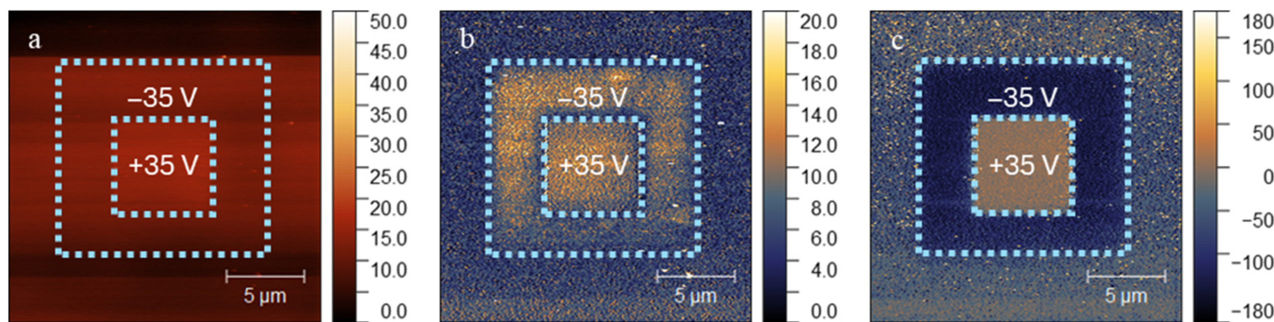

Fig. 8 Square-in-square DC poling (±35 V) PFM (a) topographical map, (b) amplitude, and (c) phase.

Open Access Article. Published on 25 Abrèll 2026. Downloaded on 29.05.26 17:53:24.
This article is licensed under a Creative Commons Attribution-NonCommercial 3.0 Unported Licence.

To further confirm ferroelectric response in ALA wurtzite AlN thin films, we perform endurance cycling (Fig. S7a) and PFM DC bias poling experiments. Weibull analysis of device failure is shown in the Supporting Information (Fig. S7b). Fig. 8b and c shows the piezoresponse amplitude and phase after square-in-square DC poling at ± 35 V, respectively. The regions in which poling induced changes in piezoresponse are marked in the PFM maps with dotted rectangles. We observe higher magnitude piezoresponse amplitude in the poled regions (Fig. 8b), while the piezoresponse phase is reversed in the two square-in-square regions (Fig. 8c). This corresponds to oppositely oriented polarization domains in the AlN film. We emphasize that while PFM mapping measurements on their own do not probe ferroelectricity as piezoresponse is a characteristic of all piezoelectric materials,[21] the present results involve DC bias poling experiments. When a DC external electric field is applied to a piezoelectric material, polarization and strain increase simultaneously, responding in concert. However, when the DC external electric field is removed, a piezoelectric material cannot sustain the polarization and strain. On the other hand, a ferroelectric material has a remanent polarization (and strain) when an external applied electric field is removed. Thus, the PFM observations are consistent with the piezoresponse expected from a ferroelectric material. We qualify this observation with the caveat that artifacts related to charging or ionic mobility can also give rise to ferroelectric behavior in PFM measurements.[47] Finally, the P_r of ALA wurtzite AlN devices exhibits little dependence on device size (Fig. S8). For larger top electrodes, P_r is largely constant, indicating that switching charge scales with capacitor area and is not dominated by perimeter/conductive filaments. For the smallest top electrode size, an increase in P_r is observed (Fig. S8). To rationalize this, consider that if structural defects have a uniform spatial distribution, then smaller top electrode devices have fewer expected structural defects.

Though high leakage currents and sub-optimal endurance currently limit application of high polarization ferroelectrics, the unique memory architectures offered by their distinctive properties warrants further investigation and refinement. In-memory computing is one highly promising potential application for AlN-based ferroelectric devices. Leveraging a non-von Neumann architecture to remove the separation of the central processing unit and memory enables significant improvements to performance and efficiency of data-intensive computations through the potential for fast read/write speeds and low power switching of ferroelectric devices.[48] Neuromorphic computing is a another widely-cited application of high polarization ferroelectrics, due to their high memory density and wide memory window making analog storage possible.[49,50] Another application of AlN-based ferroelectrics is in high temperature memory. Many ferroelectric materials are constrained by their ferroelectric to paraelectric phase transition temperature, or Curie temperature. Ferroelectricity has been demonstrated in AlScN at 400 °C;[51] wurtzite AlN has a theoretical Curie temperature exceeding its melting point (~2600 °C), far greater than that of conventional ferroelectrics.[52]

Conclusions

We have demonstrated growth of nanocrystalline wurtzite AlN using an ALA process using N_2 plasma that satisfies BEOL CMOS compatibility requirements. Compositional measurements show the films are nitrogen-poor. Structural characterization of the AlN films using plan-view and cross-section S/TEM clearly shows the wurtzite crystal structure. While most wurtzite AlN-based ferroelectric materials include extrinsic alloying components, the present work demonstrates ferroelectricity in wurtzite AlN with no intentional extrinsic alloying components as measured by electrical measurements (high polarization device, $2P_r \sim 70\ \mu C\ cm^{-2}$) and DC poling PFM experiments. There is some controversy regarding this, but we consider that AlScN and AlN are isostructural. We contend that, with sufficiently high dielectric breakdown field, ferroelectric switching in AlN can be achieved. With high electronic quality ALA wurtzite AlN films, we also report ferroelectric capacitor devices that do not undergo dielectric breakdown even at electric fields ~10 MV cm^{-1}. Our results show that ALA provides a promising route to wurtzite AlN-based ferroelectrics devices that warrants further study. As compared to reactive sputtering, ALD-based processes also hold significant advantages for integration with Si-based electronics from an application standpoint.

Author contributions

D. A. D.: conceptualization, investigation, formal analysis, writing (original draft), and writing (reviewing/editing). D. M. G.:

Open Access Article. Published on 25 Abrëll 2026. Downloaded on 29.05.26 17:53:24.
This article is licensed under a Creative Commons Attribution-NonCommercial 3.0 Unported Licence.

investigation and writing (reviewing/editing). I. M. K.: investigation and writing (reviewing/editing). B. B.: investigation and writing (reviewing/editing). X. Z.: investigation and writing (reviewing/editing). W. X.: investigation and writing (reviewing/editing). S. S.: investigation and writing (reviewing/editing). D. C.: investigation, formal analysis, and writing (reviewing/editing). W. J. M.: conceptualization, investigation, formal analysis, writing (reviewing/editing), and funding acquisition. A. C. M.: conceptualization, investigation, formal analysis, writing (original draft), writing (reviewing/editing), and funding acquisition. All authors have read and agreed to the published version of the manuscript.

Conflicts of interest

There are no conflicts to declare.

Data availability

The authors declare that the data supporting the findings of this study are available within the paper or in the supporting information (SI). Supplementary information includes raw data for PUND measurements, additional TEM/STEM data, device endurance measurements and is available at DOI: https://doi.org/10.1039/d6nh00035e.

Acknowledgements

This work was funded in part by the NSF EPSCoR program, under awards OIA-1541079 and OIA-1946231. We acknowledge funding from a University of Missouri Materials Science and Engineering Institute (MUMSEI) seed grant.

References

1 J. Hayden, M. D. Hossain, Y. Xiong, K. Ferri, W. Zhu, M. V. Imperatore, N. Giebink, S. Trolier-McKinstry, I. Dabo and J.-P. Maria, *Phys. Rev. Mater.*, 2021, **5**, 044412.
2 D. Wang, J. Zheng, P. Musavigharavi, W. Zhu, A. C. Foucher, S. E. Trolier-McKinstry, E. A. Stach and R. H. Olsson, *IEEE Electron Device Lett.*, 2020, **41**, 1774–1777.
3 S. Fichtner, N. Wolff, F. Lofink, L. Kienle and B. Wagner, *J. Appl. Phys.*, 2019, **125**, 114103.
4 C. Skidmore, J. Nordlander, J. Hayden, A. Rice, R. Collazo, Z. Sitar and J.-P. Maria, *J. Appl. Phys.*, 2025, **138**, 014101.
5 S. K. Ryoo, K. D. Kim, W. Choi, P. Sriboriboon, S. Heo, H. Seo, Y. H. Jang, J. W. Jeon, M. K. Yeom, S. H. Lee, H. S. Park, Y. Kim and C. S. Hwang, *Adv. Mater.*, 2025, **37**, 2413295.
6 S. Yang, D. Wang, M. M. H. Tanim, D. Wang and Z. Mi, *Appl. Phys. Lett.*, 2024, **124**, 193501.
7 N. Sun, K. Okamoto, S. Yasuoka, S. Doko, N. Matsui, T. Irisawa, K. Tsunekawa, H. Lu, A. Gruverman and H. Funakubo, *APL Mater.*, 2025, **13**, 051106.
8 B. Bhattarai, X. Zhang, W. Xu, Y. Gu, W. J. Meng and A. C. Meng, *Mater. Horiz.*, 2024, **11**, 5402–5408.
9 X. Zhang, E. A. Stach, W. J. Meng and A. C. Meng, *Nanoscale Horiz.*, 2023, **8**, 674–684.
10 Z. Han, C.-C. Chen, D. K. Pradhan, D. C. Moore, R. Gudavalli, X. Yang, K.-H. Kim, H. Cho, Z. Anderson, S. Ware, H. Yellai, W. J. Kennedy, N. R. Glavin, R. H. Olsson, III and D. Jariwala, *Device*, 2026, **4**(2), 100974.
11 Y. Gu, A. C. Meng, A. Ross and L.-Q. Chen, *J. Appl. Phys.*, 2024, **135**, 094102.
12 B. Saini, F. Huang, Y. Y. Choi, Z. Yu, J. D. Baniecki, V. Thampy, W. Tsai and P. C. McIntyre, *Solid-State Electron.*, 2023, **208**, 108714.
13 Z. Yu, B. Saini, Y. Liu, F. Huang, A. Mehta, J. D. Baniecki, H. S. P. Wong, W. Tsai and P. C. McIntyre, *ACS Appl. Mater. Interfaces*, 2022, **14**, 53057–53064.
14 M. Lederer, S. Abdulazhanov, R. Olivo, D. Lehninger, T. Kämpfe, K. Seidel and L. M. Eng, *Sci. Rep.*, 2021, **11**, 22266.
15 Z. Liu, X. Shi, J. Wang and H. Huang, *npj Quantum Mater.*, 2024, **9**, 44.
16 S. S. Fields, S. W. Smith, P. J. Ryan, S. T. Jaszewski, I. A. Brummel, A. Salanova, G. Esteves, S. L. Wolfley, M. D. Henry, P. S. Davids and J. F. Ihlefeld, *ACS Appl. Mater. Interfaces*, 2020, **12**, 26577–26585.
17 B. Zeng, S. Xie, S. Zhang, H. Huang, C. Ju, S. Zheng, Q. Peng, Q. Yang, Y. Zhou and M. Liao, *Acta Mater.*, 2024, **272**, 119920.
18 K. D. Kim, Y. B. Lee, S. H. Lee, I. S. Lee, S. K. Ryoo, S. Y. Byun, J. H. Lee and C. S. Hwang, *Nanoscale*, 2023, **15**, 16390–16402.
19 W. Yang, L. Chen, M. Li, F. Liu, X. Liu, C. Liu and J. Kang, *Appl. Phys. Lett.*, 2023, **123**, 132903.
20 J. Kataoka, S.-L. Tsai, T. Hoshii, H. Wakabayashi, K. Tsutsui and K. Kakushima, *Jpn. J. Appl. Phys.*, 2021, **60**, 030907.
21 X. Zhang, W. Xu, B. Bhattarai, D. A. Dalba, D. M. Gamachchi, I. M. Karunarathne, Y. Yu, N. J. Pravda, R. Gong, D. Stalla, C. Zu, W. J. Meng and A. C. Meng, *Ceramics*, 2025, **8**, 146.
22 M. R. Islam, N. Wolff, M. Yassine, G. Schönweger, B. Christian, H. Kohlstedt, O. Ambacher, F. Lofink, L. Kienle and S. Fichtner, *Appl. Phys. Lett.*, 2021, **118**, 232905.
23 Y. Katsumata, T. Ohguro, K. Inoh, E. Morifuji, T. Yoshitomi, H. Kimijima, H. Nii, T. Morimoto, H. S. Momose, K. Yoshikawa, H. Ishiuchi and H. Iwai, in *The VLSI Handbook*, ed. W.-K. Chen, CRC Press, New York, 2nd edn, 2006.
24 X. Zhang, W. Xu, W. J. Meng and A. C. Meng, *CrystEngComm*, 2024, **26**, 180–191.
25 C. S. Sandu, F. Parsapour, S. Mertin, V. Pashchenko, R. Matloub, T. LaGrange, B. Heinz and P. Muralt, *Phys. Status Solidi A*, 2019, **216**, 1800569.
26 Y. Ji, A. Liu, R. Yan, S. Zhang and A. Gu, *J. Microelectromechanical Syst.*, 2025, **34**, 744–751.
27 R. W. Johnson, A. Hultqvist and S. F. Bent, *Mater. Today*, 2014, **17**, 236–246.
28 M. M. H. Tanim, M. T. Hasan, Z. Ye, S. Mondal, J. Liu, K. Sun and Z. Mi, *Appl. Phys. Lett.*, 2025, **127**, 032109.

 This journal is © The Royal Society of Chemistry 2026

Open Access Article. Published on 25 Abrëll 2026. Downloaded on 29.05.26 17:53:24.
This article is licensed under a Creative Commons Attribution-NonCommercial 3.0 Unported Licence.

29 J. Lee, J. Jeon, D. Jung, Y. Lee, B. Shin, J.-H. An, J.-R. Jeong, Y.-J. Yu, H. Shin and N. Jeon, *Adv. Electron. Mater.*, 2026, **12**, e00643.
30 R. G. Parkhomenko, O. De Luca, Ł. Kołodziejczyk, E. Modin, P. Rudolf, D. Martínez Martínez, L. Cunha and M. Knez, *Dalton Trans.*, 2021, **50**, 15062–15070.
31 Y. C. Jung, S. M. Hwang, D. N. Le, A. L. N. Kondusamy, J. Mohan, S. W. Kim, J. H. Kim, A. T. Lucero, A. Ravichandran, H. S. Kim, S. J. Kim, R. Choi, J. Ahn, D. Alvarez, J. Spiegelman and J. Kim, *Materials*, 2020, **13**, 3387.
32 S. Lee, G. Lee, J. Oh and J. An, *Int. J. Precis. Eng. Manuf.*, 2025, **26**, 2551–2571.
33 E. Österlund, H. Seppänen, K. Bespalova, V. Miikkulainen and M. Paulasto-Kröckel, *J. Vac. Sci. Technol., A*, 2021, **39**, 032403.
34 S. T. Ueda, A. McLeod, D. Alvarez, D. Moser, R. Kanjolia, M. Moinpour, J. Woodruff and A. C. Kummel, *Appl. Surf. Sci.*, 2021, **554**, 149656.
35 H.-Y. Shih, W.-H. Lee, W.-C. Kao, Y.-C. Chuang, R.-M. Lin, H.-C. Lin, M. Shiojiri and M.-J. Chen, *Sci. Rep.*, 2017, **7**, 39717.
36 V. K. Gogi, C. Chae, A. Barua, J. Hwang and R. Jha, *APL Mater.*, 2025, **13**, 051122.
37 W. Zhu, J. Hayden, F. He, J.-I. Yang, P. Tipsawat, M. D. Hossain, J.-P. Maria and S. Trolier-McKinstry, *Appl. Phys. Lett.*, 2021, **119**, 062901.
38 R. H. Olsson, Z. Tang and M. D. Agati, *Year*.
39 V. K. Gogi, S. Barve, A. Jones and R. Jha, *Year*.
40 R. M. R. Pinto, V. Gund, R. A. Dias, K. K. Nagaraja and K. B. Vinayakumar, *J. Microelectromechanical Syst.*, 2022, **31**, 500–523.
41 Y. Ohtsu, T. Tabaru and J. Schulze, *J. Vac. Sci. Technol., B*, 2024, **42**, 044204.
42 S. Berg and I. V. Katardjiev, *J. Vac. Sci. Technol., A*, 1999, **17**, 1916–1925.
43 D. A. Dalba, S. Saadat Niavol, X. Zhang, W. Xu, B. Bhattarai, I. M. Karunarathne, D. M. Gamachchi, D. Cao, W. J. Meng and A. C. Meng, *J. Vac. Sci. Technol., B*, 2025, **43**, 022207.
44 F. Huang, B. Saini, L. Wan, H. Lu, X. He, S. Qin, W. Tsai, A. Gruverman, A. C. Meng, H. S. P. Wong, P. C. McIntyre and S. Wong, *ACS Nano*, 2024, **18**, 17600–17610.
45 A. Ghobadi, S. S. Niavol, E. Restuccia, A. C. Meng and S. Guha, *Appl. Phys. Lett.*, 2024, **124**, 153301.
46 D. M. Gamachchi, I. M. Karunarathne, A. Negi, S. S. Niavol, D. A. Dalba, X. Zhang, W. Xu, S. Guha, W. J. Meng and A. C. Meng, *MRS Commun.*, 2026, DOI: 10.1557/s43579-026-00960-9.
47 N. Balke, P. Maksymovych, S. Jesse, A. Herklotz, A. Tselev, C.-B. Eom, I. I. Kravchenko, P. Yu and S. V. Kalinin, *ACS Nano*, 2015, **9**, 6484–6492.
48 H. Zhou, S. Li, K. W. Ang and Y. W. Zhang, *Nano-Micro Lett.*, 2024, **16**, 121.
49 T. Mikolajick, M. H. Park, L. Begon-Lours and S. Slesazeck, *Adv. Mater.*, 2023, **35**, 2206042.
50 E. Covi, H. Mulaosmanovic, B. Max, S. Slesazeck and T. Mikolajick, *Neuromorphic Comput. Eng.*, 2022, **2**, 012002.
51 D. Drury, K. Yazawa, A. Zakutayev, B. Hanrahan and G. Brennecka, *Micromachines*, 2022, **13**, 887.
52 U. De, K. R. Sahu and A. De, *Solid State Phenom.*, 2015, **232**, 235–278.